

# *i*-MXenes for Energy Storage and Catalysis

Bilal Ahmed,\* Ahmed El Ghazaly, and Johanna Rosen\*

In 2017, a new family of in-plane, chemically-ordered quaternary MAX phases, coined *i*-MAX, has been reported since 2017. The first *i*-MAX phase,  $(\text{Mo}_{2/3}\text{Sc}_{1/3})_2\text{AlC}$ , garnered significant research attention due to the presence of chemically ordered Sc within the Mo-dominated M layer, and the facilitated removal of both Al and Sc upon etching, resulting in 2D *i*-MXene,  $\text{Mo}_{1.33}\text{C}$ , with ordered divacancies. The *i*-MXene renders an exceptionally low resistivity of  $33.2 \mu\Omega \text{ m}^{-1}$  and a high volumetric capacitance of  $\approx 1150 \text{ F cm}^{-3}$ . This discovery has been followed by the synthesis of, to date, 32 *i*-MAX phases and 5 *i*-MXenes, where the latter have shown potential for applications including, but not limited to, energy storage and catalysis. Herein, fundamental investigations of *i*-MAX phases and *i*-MXenes, along with their applicability in supercapacitive and catalytic applications, are reviewed. Moreover, recent results on ion intercalation and post-etching treatment of  $\text{Mo}_{1.33}\text{C}$  are presented. The charge storage performance can also be tuned by forming MXene hydrogel and through inert atmosphere annealing, where the latter renders a superior volumetric capacitance of  $\approx 1635 \text{ F cm}^{-3}$ . This report demonstrates the potential of the *i*-MXene family for catalytic and energy storage applications, and highlights novel research directions for further development and successful employment in practical applications.

are widely investigated due to their high electrical and thermal conductivity, excellent damage tolerance, lightweight, and high-temperature strength.<sup>[5b,7]</sup> Moreover, the self-healing characteristics, reversible deformation, and magnetic properties of MAX phases have further spurred the interest in this large family, which to date consists of  $\approx 155$  members with 16 A elements and 14 M elements.<sup>[5,7,8]</sup>

In addition to the conventional ternary MAX phases, the possibility of alloying on the M, A, or X sites is of utmost importance from the application and scientific viewpoints.<sup>[9]</sup> The incorporation of additional elements enables tuning of properties and the formation of non-conventional MAX phases.<sup>[9e,10]</sup> Typically, alloying of a MAX phase results in chemically disordered solid solutions, for example,  $(\text{Cr,Mn})_2\text{AlC}$ <sup>[11]</sup> and  $(\text{Mo}_{0.5}\text{Mn}_{0.5})_2\text{GaC}$ .<sup>[12]</sup> It has also been demonstrated that MAX phase alloys can display chemically ordered structures. To date, two types of chemical ordering have

## 1. Introduction

The multitude of compositions and structures of 2D layered materials render promise for next-generation energy storage,<sup>[1]</sup> thermoelectric,<sup>[2]</sup> catalytic,<sup>[3]</sup> and memory devices.<sup>[4]</sup> Recently, atomically laminated ceramics, known as MAX phases,<sup>[5]</sup> have garnered increased attention due to the discovery of so-called MXenes.<sup>[6]</sup> The latter are 2D transition metal carbides and nitrides derived by selectively removing the A-layer from the parent  $\text{M}_{n+1}\text{AX}_n$  (MAX) phases, where M corresponds to a transition metal, A refers to an A-group element like Si, Al, or Ga, and X denotes carbon (C) or nitrogen (N), and  $n = 1-4$ . The MAX phases exhibit ceramic-metallic hybrid characteristics, and

been observed in MAX phases; out-of-plane chemical order (*o*-MAX) and in-plane chemical order (*i*-MAX), both with M element ordering.<sup>[13]</sup> *o*-MAX phases have a sandwich-like stacking with the two M-elements separated in distinct layers, for example,  $\text{TiCr}_2\text{AlC}_2$ <sup>[14]</sup> and  $\text{TiMo}_2\text{AlC}_2$ .<sup>[15]</sup> The stability of these phases can be ascribed to multiple M sites, which can hinder energetically unfavorable stacking of M and C, and a higher electronegativity of M, which renders fewer electrons available for antibonding Al-Al orbitals.<sup>[13a,16]</sup> As opposed to *o*-MAX, *i*-MAX phases exhibit in-plane chemical ordering of two M elements in a 2:1 ratio, with a generic formula of  $(\text{M}_{2/3}^1\text{M}_{1/3}^2)_2\text{AC}$ , where A to date has been either Al or Ga.<sup>[13b,16b]</sup> One of the main features of the *i*-MAX phases is the possibility for selective removal of Al as well as the  $\text{M}^2$  elements upon etching, resulting in a 2D MXene structure with ordered vacancies, also sometimes referred to as *i*-MXene.<sup>[13b,17]</sup> The first member of the *i*-MAX family was  $(\text{Mo}_{2/3}\text{Sc}_{1/3})_2\text{AlC}$ , and its *i*-MXene  $\text{Mo}_{1.33}\text{C}$  rendered a high volumetric capacitance of  $\approx 1150 \text{ F cm}^{-3}$ .<sup>[17]</sup> Inspired by these first results, we have investigated a variety of *i*-MAX phase and *i*-MXenes, theoretically and experimentally, and have demonstrated their potential for a range of applications.

Herein, we summarize our recent progress in the development of *i*-MXenes for energy storage and catalytic applications. First, we present an overview of the structure and composition of the parent *i*-MAX phases, followed by a detailed description of the corresponding MXenes. Then, we summarize the

Dr. B. Ahmed, A. El Ghazaly, Prof. J. Rosen  
Thin Film Physics Division  
Department of Physics, Chemistry, and Biology (IFM)  
Linköping University  
Linköping SE-583 31, Sweden  
E-mail: bilal.ahmed@liu.se; johanna.rosen@liu.se

The ORCID identification number(s) for the author(s) of this article can be found under <https://doi.org/10.1002/adfm.202000894>.

© 2020 The Authors. Published by WILEY-VCH Verlag GmbH & Co. KGaA, Weinheim. This is an open access article under the terms of the Creative Commons Attribution License, which permits use, distribution and reproduction in any medium, provided the original work is properly cited.

DOI: 10.1002/adfm.202000894

reported investigations, to date, of *i*-MXenes in the areas of energy storage and catalysis. Moreover, we also present some of our most recent results, and highlight the promise of these unique materials for energy storage applications.

## 2. Discovery of the *i*-MAX Phases and Structural Characteristics

The first indication of an *i*-MAX phase was observed during the structural characterization of a sample also containing the  $\text{Mo}_2\text{ScAlC}_2$  *o*-MAX phase.<sup>[18]</sup> However, as theoretical studies have demonstrated that both  $\text{Mo}_2\text{AlC}$  and  $\text{Sc}_2\text{AlC}$  are unstable, and hence not likely to be experimentally observed, a  $(\text{Mo,Sc})_2\text{AlC}$  solid solution was initially expected.<sup>[17]</sup> Still, owing to the large Z contrast between Mo and Sc atoms, in-plane chemical order could be observed between the M elements by using high-resolution scanning transmission electron microscopy (HRSTEM). The chemical composition of the first in-plane chemically ordered MAX phase was  $(\text{Mo}_{2/3}\text{Sc}_{1/3})_2\text{AlC}$ ,<sup>[17]</sup> and detailed structural analysis revealed that the as-synthesized  $(\text{Mo}_{2/3}\text{Sc}_{1/3})_2\text{AlC}_2$  phase displays a monoclinic structure of the space group  $\text{C2/c}$  (#15).<sup>[17]</sup> It should be noted that conventional MAX phases exhibit a hexagonal structure of the space group  $\text{P6}_3/\text{mmc}$ .<sup>[5b]</sup> The crystal structure of  $(\text{Mo}_{2/3}\text{Sc}_{1/3})_2\text{AlC}_2$  has more recently been verified by X-ray diffraction (XRD), coupled with Rietveld refinement, and neutron diffraction analysis.<sup>[17,19]</sup>

The origin of *i*-MAX formation has been investigated by a combination of first-principles theoretical calculations and experimental synthesis, using  $(\text{Mo}_{2/3}\text{Sc}_{1/3})_2\text{AlC}$  and  $(\text{Mo}_{2/3}\text{Y}_{1/3})_2\text{AlC}$  as model systems.<sup>[16a]</sup> Elements from group 13 (Al, Ga, In) and group 14 (Si, Ge, Sn) have been adopted as A-layer, and seven novel *i*-MAX phases were predicted thermodynamically stable, out of which two phases were experimentally verified,  $(\text{V}_{2/3}\text{Zr}_{1/3})_2\text{AlC}$  and  $(\text{Mo}_{2/3}\text{Y}_{1/3})_2\text{AlC}$ . It was concluded that the formation of *i*-MAX requires i) an  $\text{M}^1/\text{M}^2$  ratio of 2:1, ii) a size difference between  $\text{M}^1$  and  $\text{M}^2$  of at least 0.2 Å ( $\text{M}^2 > \text{M}^1$ ), iii) an electron population of ideally bonding orbitals only, and iv) a small-sized A.<sup>[16a]</sup> From a structural viewpoint, the  $\text{M}^1$  atoms form a honeycomb lattice, whereas the  $\text{M}^2$  atoms prefer to reside at the hexagonal center, at least partly explaining the observed ideal  $\text{M}^1/\text{M}^2$  ratio of 2:1.<sup>[16]</sup> Furthermore, the  $\text{M}^2$  atoms extend from the M-layer, approaching the A-layer, which in turn rearrange to form a Kagomé-like lattice.

The differences between the atomic structure of a typical MAX phase and an *i*-MAX phase are schematically illustrated in **Figure 1**, using  $(\text{V}_{2/3}\text{Zr}_{1/3})_2\text{AlC}$  as a model. Even though the top view of both the MAX and the *i*-MAX phases indicates that the M layer ( $\text{M}^1 + \text{M}^2$ ) forms a hexagonal pattern (Figure 1a), the side view indicates that V and Zr in the *i*-MAX reside in different layers. Consequently, the hexagonal pattern can be observed in all layers of the MAX phase, whereas it is only found in the carbon layer of the *i*-MAX phase (Figure 1c). The major structural difference between MAX and *i*-MAX, however, is rendered by the Al layer (Figure 1b), where A-layer forms a hexagonal arrangement in a typical MAX phase but resembles a Kagomé-like lattice in the case of *i*-MAX. It is worth mentioning that small undulations or ripples can be observed in the Kagomé-like lattice, which can be ascribed to the atomic size difference between  $\text{M}^2$  and  $\text{M}^1$ , where the larger-sized  $\text{M}^2$



**Bilal Ahmed** received his doctoral degree in Materials Science and Engineering from King Abdullah University of Science and Technology (KAUST), Saudi Arabia, and currently works as a researcher in the Thin Film Physics Division, Linköping University, Sweden. His research interests include electrochemical energy

storage in general and Li-ion batteries and supercapacitors in particular.



**Ahmed El Ghazaly** received his MSc (2017) in Nanotechnology from the American University in Cairo, Egypt. He worked as a visiting researcher at the Department of Materials Science and Engineering at Georgia Institute of Technology, USA. He is currently pursuing doctoral studies in the physics of materials at

Linköping University (Sweden) under the supervision of Prof. Johanna Rosen. His research is focused on MXene synthesis and its energy storage applications.



**Johanna Rosen** is the head of the Materials Design Group in the Department of Physics, Chemistry, and Biology (IFM) at Linköping University. She received her Ph.D. from RWTH-Aachen University in Germany, and after being a post-doc and visiting scientist at LBNL at Berkeley (USA) and Sydney University (Australia), she

returned to Sweden to establish her research platform. Her research interest is theoretical and experimental studies targeting novel 3D and 2D materials for studying, for example, magnetism, energy storage, and catalysis. She is also researching plasma process development for thin-film synthesis, mainly focusing on magnetic materials and hard and wear-resistant coatings.

is pushed out of the  $\text{M}^1$  layer toward the Al layer.<sup>[16b]</sup> To date, we have experimentally verified 32 *i*-MAX phases, including  $(\text{Mo}_{2/3}\text{Sc}_{1/3})_2\text{AlC}$ ,<sup>[17]</sup>  $(\text{Cr}_{2/3}\text{Sc}_{1/3})_2\text{AlC}$ ,<sup>[20]</sup>  $(\text{Cr}_{2/3}\text{Y}_{1/3})_2\text{AlC}$ ,<sup>[20]</sup>  $(\text{Mo}_{2/3}\text{Y}_{1/3})_2\text{AlC}$ ,<sup>[16b]</sup>  $(\text{V}_{2/3}\text{Zr}_{1/3})_2\text{AlC}$ ,<sup>[16b]</sup>  $(\text{V}_{2/3}\text{Sc}_{1/3})_2\text{AlC}$ ,<sup>[21]</sup>



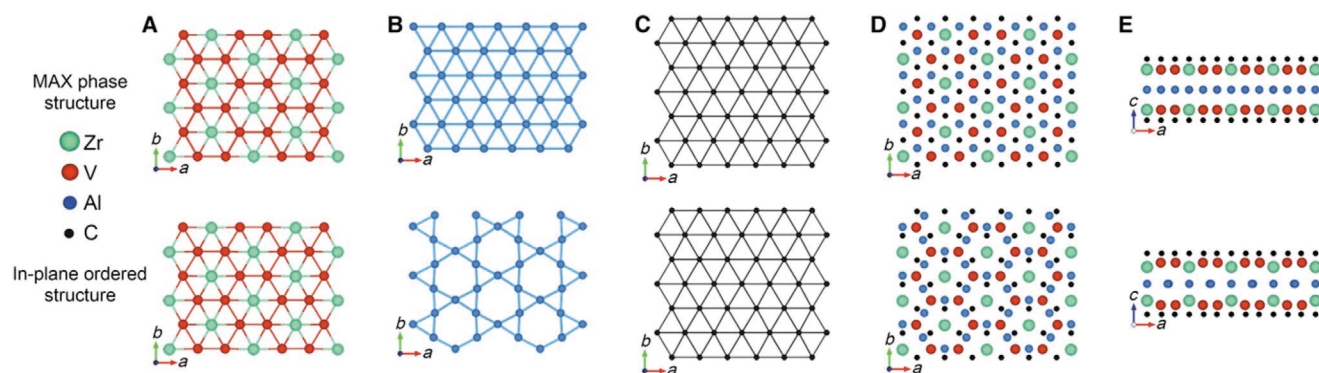


**Figure 1.** Structure of *i*-MAX phases: Comparison between a typical MAX phase (top) and *i*-MAX structures by using  $(V_{2/3}Zr_{1/3})_2AlC$ , where A) M-layer (V and Zr), B) Al-layer, and C) C-layer. D) Top-view of C-M-Al-M-C block and E) side-view of C-M-Al-M-C block. Reproduced with permission.<sup>[16b]</sup> Copyright 2017, AAAS.

$(W_{2/3}Sc_{1/3})_2AlC$ ,<sup>[22]</sup>  $(W_{2/3}Y_{1/3})_2AlC$ ,<sup>[22]</sup>  $(Cr_{2/3}Zr_{1/3})_2AlC$ ,<sup>[23]</sup>  $(Mo_{2/3}Sc_{1/3})_2GaC$ ,<sup>[16a]</sup> and  $(Mo_{2/3}Y_{1/3})_2GaC$ .<sup>[16a]</sup>

More recently, we have also synthesized *i*-MAX phases based on rare earth (RE) elements, such as  $(Mo_{2/3}RE_{1/3})_2AlC$ , where RE = Ce, Pr, Nd, Sm, Gd, Tb, Dy, Ho, Er, Tm, and Lu, unraveling complex magnetic properties.<sup>[24]</sup> The magnetic transition temperatures has been found to be < 30 K, which can be compared to Mn-based MAX phases, such as  $Mn_2GaC$  and  $(Mn_{0.5}Cr_{0.5})_2GaC$ , exhibiting transition temperatures of up to  $\approx 500$  K.<sup>[25]</sup> In addition, Petruhins et al. utilized a theoretical-experimental approach to identify and synthesize Cr- and Mn-based *i*-MAX phases, targeting superior magnetic properties,<sup>[26]</sup> which remains to be investigated. **Figure 2a,b** show HRSTEM

images of  $(Cr_{2/3}Sc_{1/3})_2GaC$  viewed along [100] and [110] zone axes, respectively, and schematic illustrations corresponding to an orthorhombic structure of the space group  $Cmcm$  (#63). **Figure 2g,h** show the HRSTEM images of  $(Mn_{2/3}Sc_{1/3})_2GaC$  viewed along [100] and [110] zone axes, respectively. One should note that the structure of a traditional MAX phase, viewed along  $[11\bar{2}0]$ , looks identical to the structure of *i*-MAX along the [100] direction. This is in contrast to the HRSTEM image viewed along [110] axis, showing a clear contrast between Sc and Cr/Mn atoms, and confirming the presence of chemical order in the M-layer.

It is worth emphasizing that the composition of the *i*-MAX phase renders a significant influence on the formation and

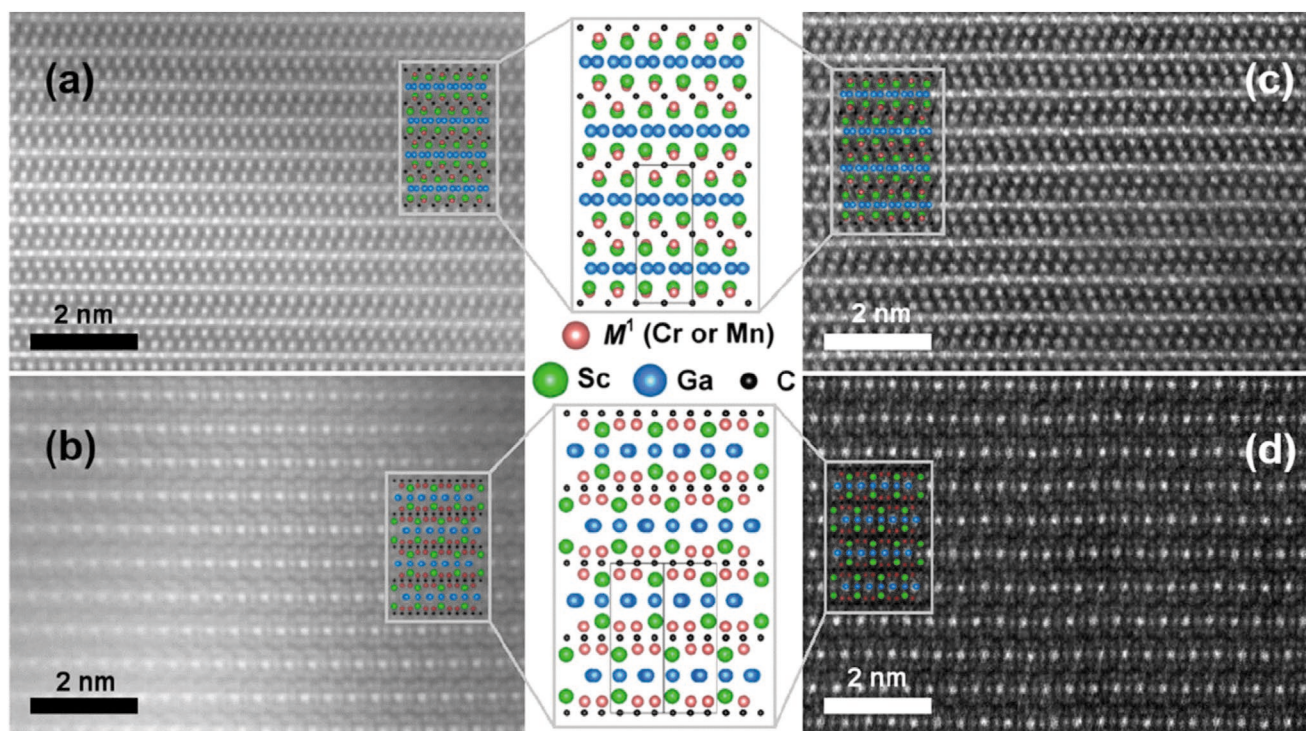


**Figure 2.** HRSTEM images of  $(Cr_{2/3}Sc_{1/3})_2GaC$  viewed along zone axes a) [100] and c) [110], and  $(Mn_{2/3}Sc_{1/3})_2GaC$  viewed along zone axes b) [100] and d) [110], where the schematic illustrations are based on the atomic arrangement in an orthorhombic structure with a space group  $Cmcm$ . Reproduced with permission.<sup>[26]</sup> Copyright 2020, American Chemical Society.

properties of the derived *i*-MXene. For example, Mockute et al.<sup>[19]</sup> used density functional theory (DFT) calculations and neutron diffraction analysis to explore the phase stability and possible M-site intermixing between Mo/Sc in the *i*-MAX phase ( $\text{Mo}_x\text{Sc}_{1-x}\text{AlC}$ ). An *i*-MAX structure is found to be retained with increasing Sc content (i.e.,  $x < 0.66$ ), where excessive Sc occupies the Mo sites. Still, it is also demonstrated that the corresponding *i*-MXene is only obtained for  $x = 0.66$ , that is, the ideal *i*-MAX stoichiometry, whereas  $x = 0.33$  and  $0.5$  do not allow derivation of *i*-MXene.<sup>[19]</sup> Hence, slight alternations in chemical composition of the parent *i*-MAX phase may significantly influence the existence and quality of resulting *i*-MXene.

### 3. Synthesis and Characterization of *i*-MXenes

To date, there are reports on the synthesis of *i*-MAX phases with aluminum and gallium in the A-layers.<sup>[16a,17]</sup> However, the corresponding *i*-MXenes have only been obtained for A = Al, by using the conventional MAX phase etching routes with some minor modifications. Nonetheless, and most importantly, for etching of  $(\text{Mo}_{2/3}\text{Sc}_{1/3})_2\text{AlC}_2$ , both the Al and Sc are selectively removed by either HF treatment or LiF/HCl treatment, resulting in 2D  $\text{Mo}_{1.33}\text{C}$  MXene with ordered divacancies.<sup>[17]</sup> Similarly, for  $(\text{W}_{2/3}\text{Sc}_{1/3})_2\text{AlC}$  and  $(\text{W}_{2/3}\text{Y}_{1/3})_2\text{AlC}$ , both Al and Sc (Y) were selectively removed to obtain  $\text{W}_{1.33}\text{C}$  MXenes with ordered divacancies.<sup>[22]</sup> The synthesis of *i*-MXene is schematically illustrated in Figure 3, where delamination of the multilayer *i*-MXene is carried out by using an organic base, for example, tetrabutylammonium hydroxide (TBAOH), to obtain free-standing *i*-MXene sheets which after filtration can be used for characterization and as working electrodes in energy storage devices.

The *i*-MAX phases also facilitate what we have called “targeted etching”, that is, where the A-layer of the *i*-MAX phase can be etched without removal of the M<sup>2</sup>-layer, see Figure 4. This is achieved by a tuned etching process, and leads to the formation of in-plane chemically ordered MXene without inherent vacancies.<sup>[28]</sup> This has been experimentally verified for  $(\text{Mo}_{2/3}\text{Y}_{1/3})_2\text{AlC}$ , which after etching of the Al layer results in chemically ordered  $(\text{Mo}_{2/3}\text{Y}_{1/3})_2\text{C}$  *i*-MXene. The same *i*-MAX phase can also be etched into a vacancy-ordered  $\text{Mo}_{1.33}\text{C}$  *i*-MXene (Figure 4). It can be noted that under-etching of a conventional MAX phase results in a mixture of MAX and MXene phases,<sup>[6a]</sup> whereas over-etching results in (partial) removal of both M- and A-layers, leading to the formation of

carbide-derived carbons.<sup>[29]</sup> Hence, the synthesis of *i*-MXene, with both M<sup>1</sup> and M<sup>2</sup>, is of great significance for practical applications. For instance, it has been reported that the typical  $\text{Ti}_3\text{C}_2$  and  $\text{Ti}_2\text{C}$  MXenes can be oxidized for the in situ growth of  $\text{TiO}_2$  on the MXene surface.<sup>[30]</sup> Similarly, the oxidation of  $\text{Nb}_2\text{C}$ <sup>[31]</sup> and  $\text{V}_2\text{C}$ <sup>[32]</sup> MXenes results in the formation of  $\text{Nb}_2\text{O}_5$  and  $\text{VO}_x$  on the MXene surface, respectively. This is of importance, as the in situ grown oxides have shown significantly improved electrochemical performance in Li-ion batteries, Na-ion batteries and supercapacitors (SCs).<sup>[30,33]</sup> Hence, the utilization of *i*-MXene, with both M<sup>1</sup> and M<sup>2</sup> elements, may realize the formation of dual oxides on the MXene surface, which further expands the ability of compositional tailoring, and widening the applications horizon of *i*-MXenes.

*i*-MXenes with ordered vacancies are derived from chemically ordered *i*-MAX phases. A similar composition of Nb-based MXene ( $\text{Nb}_{1.33}\text{C}$ ) has been obtained by etching A- and M<sup>2</sup>-elements from a quaternary solid-solution  $(\text{Nb}_{2/3}\text{Sc}_{1/3})_2\text{AlC}$  MAX phase.<sup>[34]</sup> Even though  $\text{Nb}_{1.33}\text{C}$  has an M:C ratio similar to an *i*-MXene with vacancies, it has disordered vacancies and small vacancy clusters, which is also of significance for the applicability of the material. Hence, both *i*-MXene with ordered vacancies and traditional MXene with disordered vacancies can be obtained from the etching of specific quaternary MAX phase alloys, with the removal of both the A-layer and the alloying element.

The *i*-MXenes reported to date have been characterized with HRSTEM to visualize the atomic arrangement and *in-plane* order. For instance, Tao et al.<sup>[17]</sup> verified the structure of  $\text{Mo}_{1.33}\text{C}$  MXene by using HRSTEM imaging, demonstrating an excellent consistency between the experimentally observed atomic arrangement and the simulated structure of the parent phase excluding Sc and Al atoms. A similar analysis has been carried out for  $\text{W}_{1.33}\text{C}$ <sup>[22]</sup> and  $(\text{Mo}_{2/3}\text{Y}_{1/3})_2\text{C}$  *i*-MXenes.<sup>[28]</sup> Furthermore, Lind et al.<sup>[35]</sup> utilized a combination of first-principles calculations and X-ray photoelectron spectroscopy (XPS) to investigate the surface chemistry and influence of surface terminations on structure, stability, bonding and electronic properties of  $\text{Mo}_{1.33}\text{C}$  MXene. The results consistently revealed the presence of  $-\text{F}$ ,  $-\text{OH}$ , and  $-\text{O}$  surface terminations after HF etching and TBAOH delamination. Moreover, the quantitative analysis rendered a chemical formula of  $\text{Mo}_{1.2}\text{CO}_{0.7}(\text{OH})_{0.5}\text{F}_{1.1}$ , indicating the presence of F as the main surface terminations. Moreover, DFT calculations revealed that the O-terminated surface was unstable due to the unavailability of sufficient electrons due to the vacancy

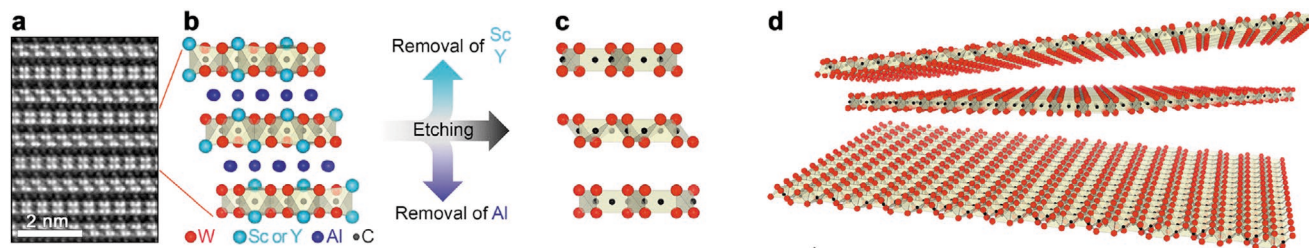


**Figure 3.** a) HRSTEM image of  $(\text{W}_{2/3}\text{Sc}_{1/3})_2\text{AlC}$  along the [100] zone axis. Schematics showing b) in-plane chemical ordering in  $(\text{W}_{2/3}\text{Sc}_{1/3})_2\text{AlC}$  or  $(\text{W}_{2/3}\text{Y}_{1/3})_2\text{AlC}$  *i*-MAX phases, c) leading to  $\text{W}_{1.33}\text{C}$  MXene with ordered divacancies after selective etching, and d) delamination. Reproduced with permission.<sup>[27]</sup> Copyright 2019, American Chemical Society.



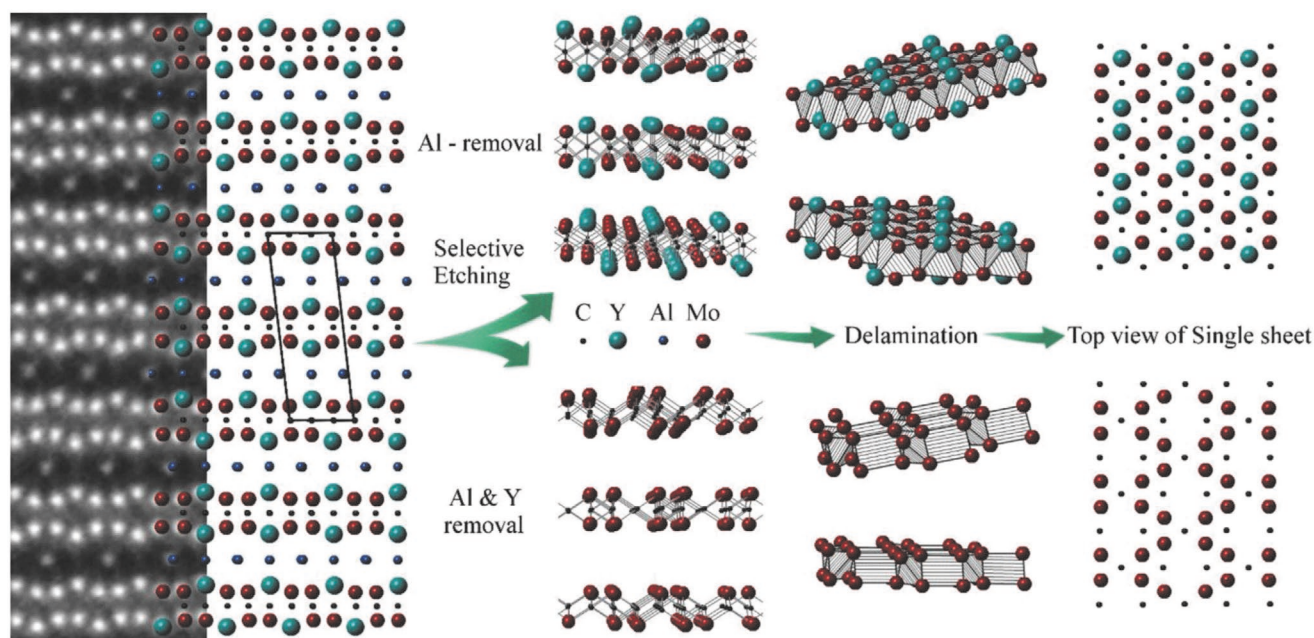


**Figure 4.** (Left) STEM image of  $(\text{Mo}_{2/3}\text{Y}_{1/3})_2\text{AlC}$ , viewed along  $[110]$  zone axis, and corresponding structure model before etching. (Middle) Depending on the etching protocol, two different structures are obtained: one in which only Al is removed (top) or one in which both Al and Y are removed (bottom). (Right) Top view of corresponding structures. Reproduced with permission.<sup>[28]</sup> Copyright 2018, Wiley-VCH.

formation, whereas the F-terminated surface, with only one additional electron, stabilized the structure.<sup>[35]</sup> In addition to the structural stability, the electronic properties of  $\text{Mo}_{1.33}\text{C}$  MXene were also influenced by surface terminations, where the Fermi level was dominated by Mo orbitals and orbitals of O and F remained at lower energies. The transport properties of Mo-based MXenes, including  $\text{Mo}_{1.33}\text{C}$  *i*-MXene flakes, have also been studied by Halim et al.,<sup>[36]</sup> showing that the variable range hopping within individual flakes is the rate-limiting step of the conduction mechanism. Furthermore, Tao et al. demonstrated that *d*- $\text{Mo}_{1.33}\text{C}$  “paper” renders an exceptionally low resistivity of  $33.2 \mu\Omega\cdot\text{m}$ . The 2D layered structure, ordered vacancies and superior electrical properties of *i*-MXenes make them promising candidates for energy storage and catalytic applications.

#### 4. *i*-MXenes for Energy Storage Applications

Conventional MXenes have exhibited promise for a wide range of applications, including energy storage, such as SCs,<sup>[1c,1e,37]</sup> hybrid ion capacitors,<sup>[38]</sup> Li/Na-ion batteries,<sup>[30a,33,39]</sup> electromagnetic interference shielding,<sup>[40]</sup> water purification,<sup>[41]</sup> photo- and electrocatalysis,<sup>[42]</sup> and sensors.<sup>[43]</sup> Even though *i*-MXenes is a more recent discovery, the non-conventional structure and compositions of *i*-MXenes, coupled with advanced theoretical and experimental characterization, demonstrate promise for applications such as catalysis and energy storage. We have carried out detailed studies to explore their potential for electrochemical energy storage applications, and herein, we summarize the progress on utilization of different *i*-MXenes in supercapacitor electrodes and also present some of our most recent results in this area.

As mentioned earlier, the first *i*-MXene,  $\text{Mo}_{1.33}\text{C}$ , has ordered divacancies due to the selective etching and removal of both Al and Sc. Tao et al.<sup>[17]</sup> characterized the charge storage performance of  $\text{Mo}_{1.33}\text{C}$  MXene in a three-electrode configuration by using *d*- $\text{Mo}_{1.33}\text{C}$  “paper”, Ag/AgCl and Pt wire as a working electrode, reference electrode, and counter electrode, respectively. The electrochemical performance was assessed by measuring cyclic voltammograms and galvanostatic charge/discharge curves in 1 M  $\text{H}_2\text{SO}_4$  electrolyte. The *d*- $\text{Mo}_{1.33}\text{C}$  “paper” exhibited a combination of double-layer capacitance and pseudocapacitance, as evidenced by the rectangular CV curves with broad redox peaks, respectively, see Figure 5a. Interestingly, a  $3 \mu\text{m}$  *d*- $\text{Mo}_{1.33}\text{C}$  “paper” electrode rendered an extremely high volumetric capacitance of  $1153 \text{ F cm}^{-3}$ , as shown in Figure 5b, which corresponds to a gravimetric capacitance of  $339 \text{ F g}^{-1}$  at the scan rate of  $2 \text{ mV s}^{-1}$ . The volumetric capacitance of *d*- $\text{Mo}_{1.33}\text{C}$  “paper” electrode was found to be 65% higher than the  $\text{Mo}_2\text{C}$  MXene paper, which is derived from the conventional  $\text{Mo}_2\text{Ga}_2\text{C}$  phase.<sup>[44]</sup> This was ascribed to the unique structure and presence of ordered vacancies, which in turn induce a higher concentration of F terminations. Moreover, the CV curves, measured at different scan rates, were utilized to obtain log (current) versus log (scan rate), resulting in *b*-values of 0.84–0.97, see Figure 5c. Hence, the charge storage behavior of *d*- $\text{Mo}_{1.33}\text{C}$  “paper” electrode is mainly dictated by surface-controlled capacitive reactions.

Herein, we present the intercalation of different cations, that is,  $\text{Li}^+$ ,  $\text{Na}^+$  and  $\text{K}^+$ , between  $\text{Mo}_{1.33}\text{C}$  nanosheets for a first estimate of the potential of *i*-MXenes for secondary-ion batteries and metal-ion capacitors. The *d*- $\text{Mo}_{1.33}\text{C}$  “paper” electrode was obtained from the  $(\text{Mo}_{2/3}\text{Sc}_{1/3})_2\text{AlC}$  phase and electrochemically cycled in 1 M LiOH, 1 M NaOH, and 1 M KOH electrolytes. Figure 6a presents the CV curves of  $\text{Mo}_{1.33}\text{C}$  in three different

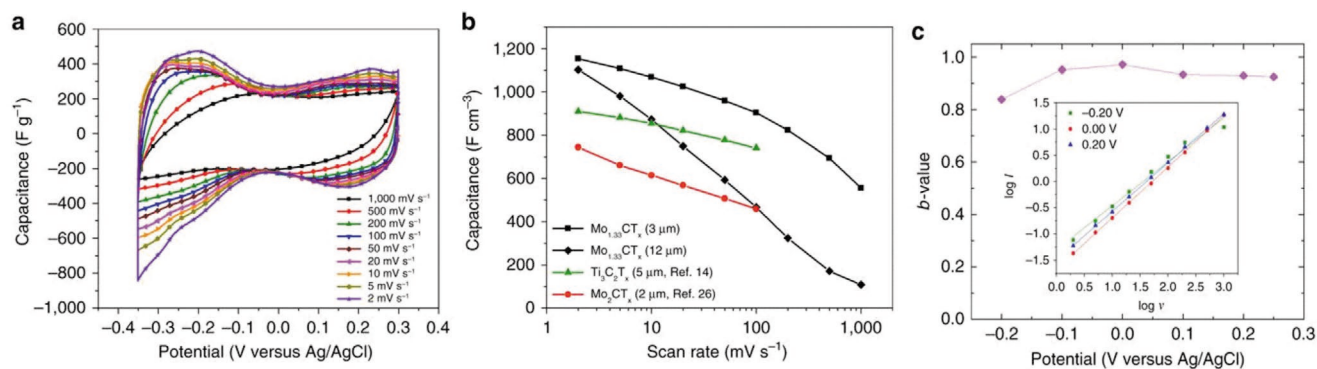


**Figure 5.** Electrochemical performance of Mo<sub>1.33</sub>C in 1M H<sub>2</sub>SO<sub>4</sub>: a) CV curves of a 3 μm-thick electrode; b) scan rate dependence of specific capacitance of 3 and 12 μm thick free-standing electrodes; and c) b values of a 3 μm-thick film, where the inset shows log I versus log scan rate. Reproduced with permission.<sup>[17]</sup> Copyright 2017, Springer Nature.

electrolytes, measured at the scan rate of 20 mV s<sup>-1</sup>. Apart from a slight difference in operating voltage window, the Mo<sub>1.33</sub>C electrode exhibited rectangular CV curves in all three electrolytes, showing surface-controlled capacitive charge storage behavior. However, the gravimetric capacitance in LiOH and NaOH electrolytes is lower than the KOH electrolyte, which indicates the easier intercalation of K-ions compared to Li- and Na-ions. The difference in intercalation behavior of the different cations between *i*-MXene sheets is similar to traditional MXenes.<sup>[45]</sup> However, further work is required to investigate this in more detail, and to establish relationships between cationic characteristics and intercalation behavior of the Mo<sub>1.33</sub>C *i*-MXene. The gravimetric capacitance of Mo<sub>1.33</sub>C electrodes in different electrolytes is plotted against the scan rate in Figure 6b. At a scan rate of 5 mV s<sup>-1</sup>, the *d*-Mo<sub>1.33</sub>C “paper” electrode exhibits a gravimetric capacitance of 89, 95, and 177 F g<sup>-1</sup> in 1 M LiOH, NaOH, and KOH electrolytes, respectively. However, at the high scan rate (500 mV s<sup>-1</sup>), the gravimetric capacitance of the Mo<sub>1.33</sub>C electrode in LiOH and NaOH electrolytes is reduced to 11 and 18 F g<sup>-1</sup>, respectively, whereas a relatively higher specific capacitance of 101 F g<sup>-1</sup> has been achieved in KOH electrolyte. These results indicate the successful intercalation of Li, Na, and K cations between *i*-MXene sheets and suggest that *i*-MXenes should be explored for secondary-ion batteries.

Various strategies have been proposed to enhance the electrochemical performance of traditional MXenes, that is, Ti<sub>3</sub>C<sub>2</sub> and Ti<sub>2</sub>C, in supercapacitive applications. For instance, MXene sheets can be decorated with electrochemically active materials, such as RuO<sub>2</sub> and MnO<sub>2</sub>, or be processed to enhance the electrolyte-accessible area by forming a 3D porous network. Herein, we present two different approaches to improve the charge storage performance of a *d*-Mo<sub>1.33</sub>C “paper” electrode: fabrication of MXene-based hydrogel, and post-etch annealing of the *i*-MXene electrodes.

The *d*-Mo<sub>1.33</sub>C “paper” was processed to form a MXene-based hydrogel (M-hydrogel), as reported elsewhere for Ti<sub>3</sub>C<sub>2</sub> MXene,<sup>[46]</sup> which resulted in an improved gravimetric capacitance of 275 F g<sup>-1</sup>, at the scan rate of 5 mV s<sup>-1</sup>, but rendered a slightly lower volumetric capacitance (1042 F cm<sup>-3</sup>) than the as-prepared *d*-Mo<sub>1.33</sub>C “paper” electrode (≈1150 F cm<sup>-3</sup>). The CV and galvanostatic charge/discharge curves of the M-hydrogel

are presented in Figure 6c, and 6d, respectively, showing a combination of double-layer capacitance and pseudocapacitance, which is consistent with the as-prepared *d*-Mo<sub>1.33</sub>C “paper”. Hence, the post-etch processing did not alter the charge storage behavior of the Mo-MXene, though the increased interlayer spacing resulted in a higher gravimetric capacitance. The cross-sectional SEM image of the M-hydrogel shows the swelling of MXene sheets (Figure 6f). Moreover, a reasonably high volumetric capacitance of 304 F cm<sup>-3</sup> was achieved at a high scan rate of 1000 mV s<sup>-1</sup>.

We also demonstrate that the annealing of Mo<sub>1.33</sub>C MXene in an argon (Ar) atmosphere, at 750 °C for 1 h, enhances the charge storage performance of *d*-Mo<sub>1.33</sub>C “paper” electrode significantly. The CV curves of the Ar-annealed *d*-Mo<sub>1.33</sub>C “paper” electrode exhibit a rectangular shape with distinct redox peaks, indicating that the charge storage occurs due to a combination of surface-controlled capacitive reactions and diffusion-controlled redox reactions, see Figure 7a. Similarly, the triangular charge/discharge curves, presented in Figure 7b, show the high potential of Ar-annealed MXene for supercapacitive applications. The Ar-treated *d*-Mo<sub>1.33</sub>C “paper” electrode rendered a superb volumetric capacitance of 1634 F cm<sup>-3</sup> at a scan rate of 2 mV s<sup>-1</sup>, and retained a volumetric capacitance of as high as 971 F cm<sup>-3</sup> at a high scan rate of 1000 mV s<sup>-1</sup>, surpassing previously reported results to date.<sup>[47]</sup> It should be noted that the CV curve, measured at 1000 mV s<sup>-1</sup>, exhibits a distinct redox couple in addition to the usual rectangular shape, while the CV curve of the as-prepared *d*-Mo<sub>1.33</sub>C “paper” electrode, measured at the scan rate of 1000 mV s<sup>-1</sup>, mainly exhibits surface-controlled capacitive behavior (Figure 6a). Hence, the as-prepared *d*-Mo<sub>1.33</sub>C “paper” electrodes, with a thickness of 3 and 12 μm, rendered a low volumetric capacitance at 1000 mV s<sup>-1</sup>. Consequently, the post-etch annealing endows superior rate capability of the Mo<sub>1.33</sub>C *i*-MXene, making it highly promising for high rate applications. As previously mentioned, the surface of the *i*-MXene is terminated with various functional groups, originating from the wet-etching procedure. It has been reported that the inert- or inert-reducing atmosphere annealing can increase the capacitive charge storage of Ti<sub>2</sub>C MXene due to the removal of undesirable surface terminations.<sup>[37b]</sup> Herein, we accordingly ascribe the improved performance of the Ar-annealed Mo<sub>1.33</sub>C to a change in MXene surface chemistry. Moreover, the *d*-Mo<sub>1.33</sub>C

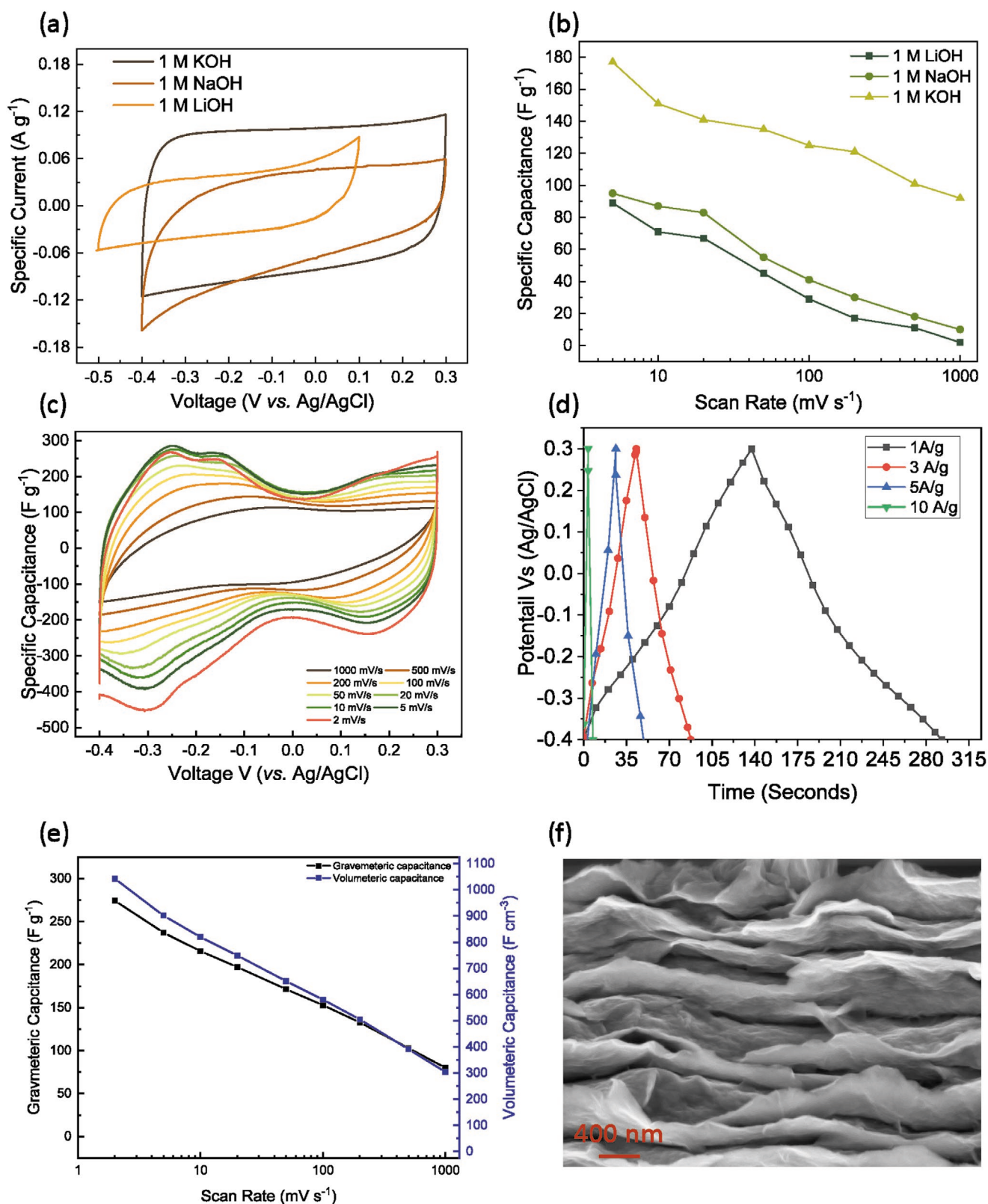


**Figure 6.** Electrochemical performance of d-Mo<sub>1.33</sub>C "paper" electrode in various aqueous electrolytes: a) CV curves in LiOH-, NaOH-, and KOH-containing electrolytes at 20 mV s<sup>-1</sup>, and b) specific capacitance versus scan rate in different electrolytes. Electrochemical performance of MXene-based hydrogel: c) CV curves at different scan rates; d) charge/discharge profiles at different current densities; e) gravimetric and volumetric capacitances versus scan rate; and f) cross-sectional SEM image of MXene-based hydrogel.



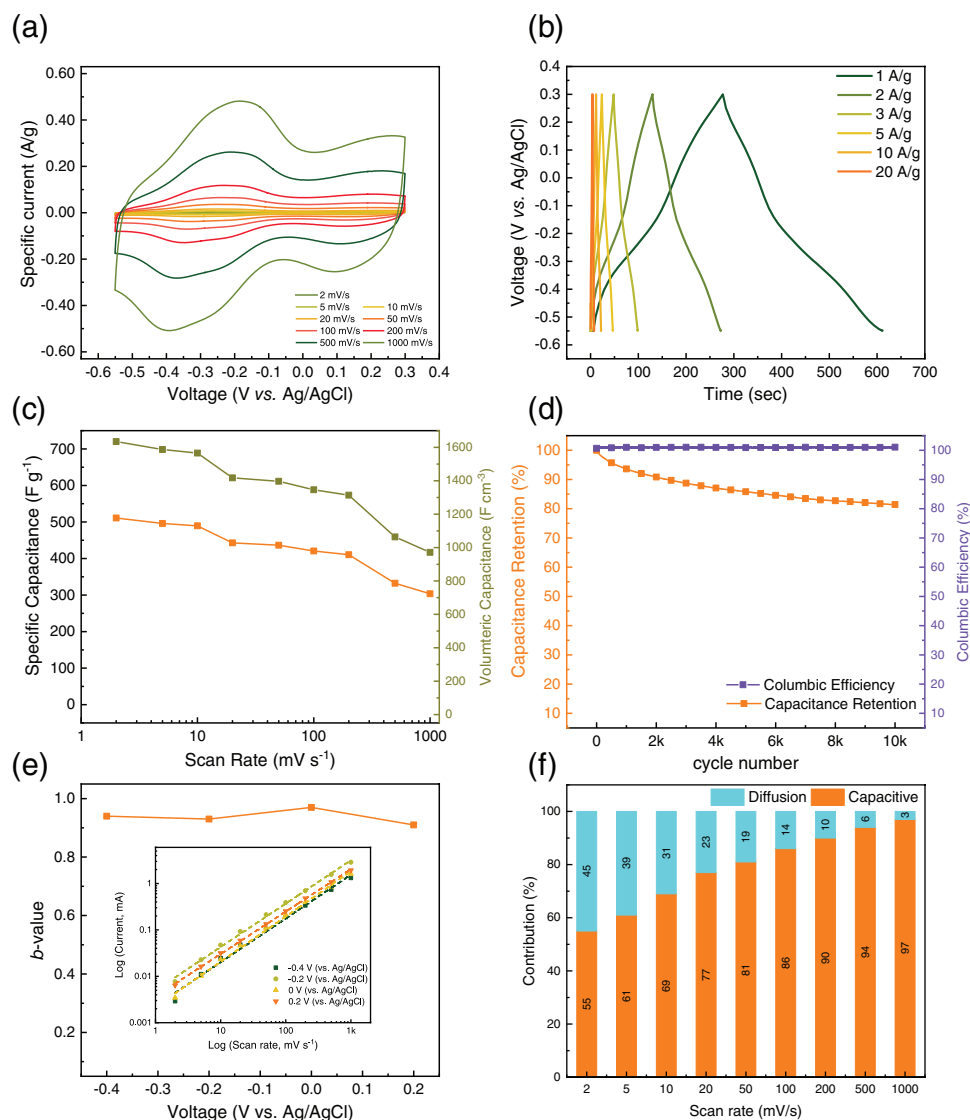


**Figure 7.** Electrochemical performance of Ar-annealed d-Mo<sub>1.33</sub>C “paper” electrode: a) CV curves at different scan rates; b) charge/discharge profiles at different current densities; c) gravimetric and volumetric capacitances versus scan rate; d) cyclic stability and coulombic efficiency; e) *b*-values at different potentials (vs Ag/AgCl), where the inset shows log *I* versus log *v*; and f) relative contribution of capacitive and diffusion currents to the total current.

“paper” electrode remained stable and retained 81.4% of the initial capacitance after 10000 charge/discharge cycles with a coulombic efficiency of almost 100%, as shown in Figure 7d.

The CV curves of the annealed MXene, measured at different scan rates, were used to decouple the surface-controlled and diffusion-controlled capacitive contributions. The relationship between CV current and scan rate can be given as:

$$I = av^b \quad (1)$$

where *I* refers to the CV current, *v* represents the scan rate and both *a* and *b* denote the fitting parameters. In general, a *b*-value of 0.5 indicates that the charge storage is determined by diffusion-controlled reactions, and a *b*-value of 1.0 indicates that the charge storage is dominated by surface-controlled capacitive reactions. The *b*-value was calculated at different potentials (vs Ag/AgCl) and was found to be in the range of 0.91 to 0.97,

see Figure 7e. Hence, the charge storage mechanism in the d-Mo<sub>1.33</sub>C “paper” electrode is a combination of diffusion- and surface-controlled processes. The capacitive and diffusion contributions can be separated by using the given equation:

$$i(V) = k_1v + k_2v^{1/2} \quad (2)$$

where *i*(*V*) refers to the current at a specific potential, *v* represents the scan rate, and *k*<sub>1</sub> and *k*<sub>2</sub> are constants. Herein, the surface-controlled capacitive contribution increased from 55% to 97% with a scan rate increased from 2 to 1000 mV s<sup>−1</sup>, respectively.

Altogether, these results show that post-etch annealing plays a critical role in enhancing the charge storage performance of these MXenes. However, further work is required to understand the influence of different annealing atmospheres on structure, surface chemistry, and electrochemical performance.



In addition to the three-electrode measurements discussed above,  $\text{Mo}_{1.33}\text{C}$ -based two-electrode symmetric and asymmetric devices have been fabricated to demonstrate the potential of  $\text{Mo}_{1.33}\text{C}$  MXene in practical applications. Qin et al.<sup>[48]</sup> fabricated two-electrode symmetric SCs by using  $\text{Mo}_{1.33}\text{C}$ /polymer composites. The electrodes for solid-state SCs were prepared by mixing  $\text{Mo}_{1.33}\text{C}$  MXene with poly(3,4-ethylenedioxythiophene):poly(styrene sulfonic acid) (PEDOT:PSS), resulting in a high-performance ultrathin, flexible  $\text{Mo}_{1.33}\text{C}$  MXene/PEDOT:PSS composite film. The flexible, solid-state SCs delivered a maximum volumetric capacitance of  $568 \text{ F cm}^{-3}$ , an ultrahigh energy density of  $33.2 \text{ mWh cm}^{-3}$  and a power density of  $19\,470 \text{ mW cm}^{-3}$ . Moreover, the  $\text{Mo}_{1.33}\text{C}$  MXene/PEDOT:PSS composite film exhibited a high volumetric capacitance of  $1310 \text{ F cm}^{-3}$  after  $\text{H}_2\text{SO}_4$  treatment. Also, the  $\text{H}_2\text{SO}_4$  treatment enhanced the rate capability of  $\text{Mo}_{1.33}\text{C}$  MXene/PEDOT:PSS composite film due to the presence of conductive PEDOT and surface redox reactions of PEDOT/MXene composite.<sup>[48]</sup>

Moreover, in situ electrochemical polymerization (EP) has been carried out to fabricate  $\text{Mo}_{1.33}\text{C}$ -doped conductive polymer films without using conventional electrolytes.<sup>[49]</sup> The colloidal solution of MXene, realized by TBAOH-assisted delamination, acted as a highly conductive solvent and facilitated the self-assembly of MXene sheets in a polymeric film, resulting in a molecular-level conjugated polymer-MXene composite films. The schematic illustration of EP-assisted EDOT polymerization and corresponding CV curves are presented in Figure 8a.<sup>[49]</sup>

Furthermore, molecular-level conjugated polymer-MXene composite films were utilized to fabricate high-performance solid-state micro-supercapacitors (MSCs), rendering excellent rate performance ( $44.1 \text{ mF cm}^{-2}$  at  $4 \text{ mA cm}^{-2}$ ), superior cyclic stability (86% after 10 000 charge/discharge cycles) and a high energy density ( $\approx 20 \text{ mWh cm}^{-3}$ ). Furthermore, asymmetric micro-supercapacitors (AMSCs) were fabricated by combining polymer-MXene composite films and  $\text{MnO}_2$  to increase the voltage and energy density of the device. The charge balance between the positive and negative electrodes was obtained by controlling the deposition time of  $\text{MnO}_2$  and thickness of E-M film, see Figure 8b. The as-fabricated AMSCs delivered an operating voltage of 1.6 V and rendered a high areal capacitance of  $69.5 \text{ mF cm}^{-2}$  ( $636.9 \text{ F cm}^{-3}$ ) at  $0.5 \text{ mA cm}^{-2}$ , as shown in Figure 8c,d, corresponding to an energy density of  $250 \text{ mWh cm}^{-3}$  at a power density of  $1.87 \text{ W cm}^{-3}$ .<sup>[49]</sup>

These studies demonstrate that electrodes of  $\text{Mo}_{1.33}\text{C}$  *i*-MXene are highly promising for capacitive energy storage applications. Nonetheless, more investigations are encouraged to explore the fundamental effect of inherent vacancies on the electrochemical charge storage mechanism. Moreover, and most important for the applicability of these materials, is that post-etching treatment and hybridization of  $\text{Mo}_{1.33}\text{C}$  with different matrices can effectively enhance the charge storage performance of  $\text{Mo}_{1.33}\text{C}$ -based symmetric and asymmetric devices even further.

While the removal of both  $\text{M}^{2-}$ - and A-layers results in the formation of  $\text{Mo}_{1.33}\text{C}$  *i*-MXene with ordered vacancies, the removal

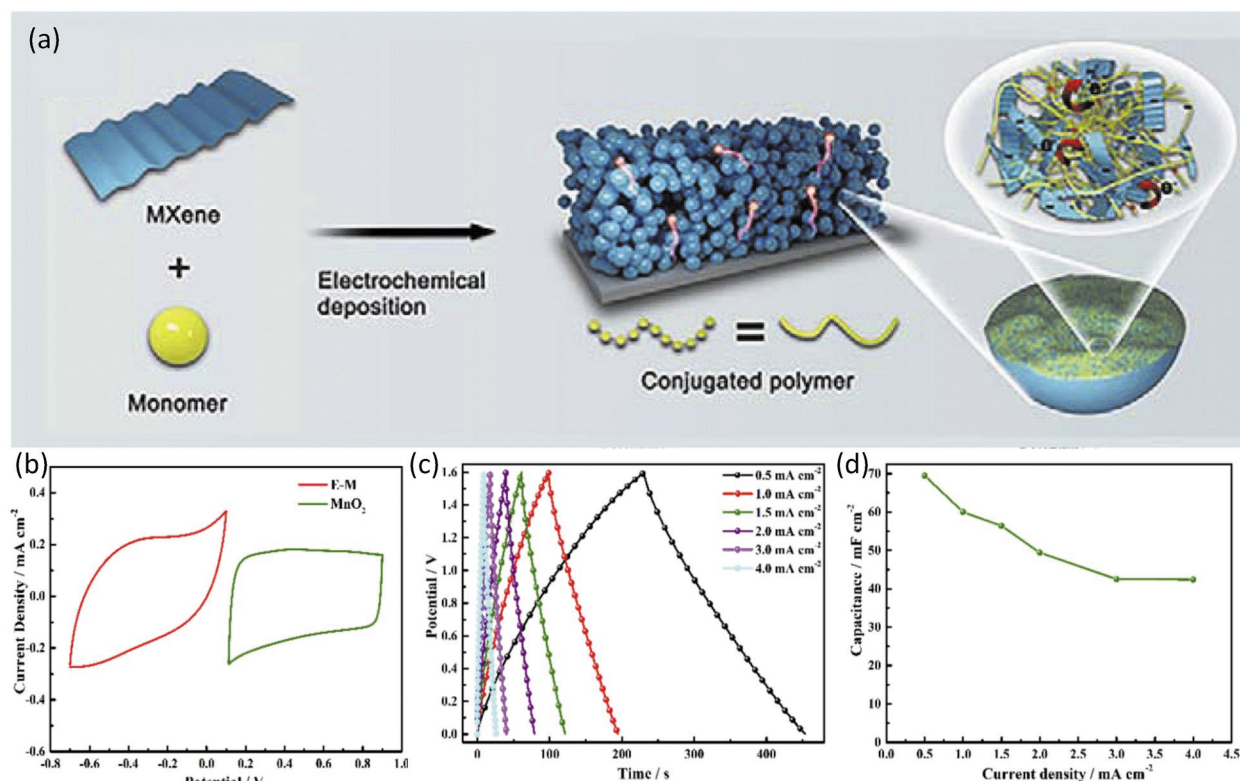


**Figure 8.** Schematic illustration of a) EP to fabricate conjugated polymer-MXene composite nanospheres; b) comparison of CV curves collected for E-M and  $\text{MnO}_2$  electrodes at a scan rate of  $100 \text{ mV s}^{-1}$ ; c) galvanostatic charge/discharge curves of AMSCs at different current densities; and d) areal specific capacitance of AMSCs at different current densities. Reproduced with permission.<sup>[49]</sup> Copyright 2019, Elsevier.

of only the A-layer from  $(\text{Mo}_{2/3}\text{Sc}_{1/3})_2\text{AlC}$  and  $(\text{Mo}_{2/3}\text{Y}_{1/3})_2\text{AlC}$  phases may result in a vacancy-free  $(\text{Mo}_{2/3}\text{Sc}_{1/3})_2\text{C}$  and  $(\text{Mo}_{2/3}\text{Y}_{1/3})_2\text{C}$  MXenes, respectively. The latter example has been experimentally verified, see Figure 4 (top panel).<sup>[28]</sup> The electrochemical characterization of a  $(\text{Mo}_{2/3}\text{Y}_{1-x/3})_2\text{C}$  “paper” electrode in  $\text{H}_2\text{SO}_4$  electrolyte rendered a volumetric capacitance of  $960 \text{ F cm}^{-3}$  ( $230 \text{ F g}^{-1}$ ) at the scan rate of  $20 \text{ mV s}^{-1}$ , which is 70% higher than  $\text{Mo}_2\text{C}$  ( $550 \text{ F cm}^{-3}$ ) but slightly lower than  $\text{Mo}_{1.33}\text{C}$  MXene with ordered vacancies ( $1150 \text{ F cm}^{-3}$ ).<sup>[28]</sup> Hence, the presence of ordered vacancies seems to play a vital role in the observed superior electrochemical performance of *i*-MXenes. Moreover, the charge storage behavior of  $(\text{Mo}_{2/3}\text{Y}_{1-x/3})_2\text{C}$  “paper” electrode has been assessed in  $6 \text{ M KOH}$  electrolyte, exhibiting a high volumetric capacitance of  $1550 \text{ F cm}^{-3}$  ( $370 \text{ F g}^{-1}$ ) and  $900 \text{ F cm}^{-3}$  at the scan rate of 2 and  $200 \text{ mV s}^{-1}$ , respectively, demonstrating an excellent rate capability of this electrode.<sup>[28]</sup>

In addition to Mo-based *i*-MXenes, we have also reported an initial evaluation of the charge storage performance of  $\text{W}_{1.33}\text{C}$  *i*-MXene, being derived from  $(\text{W}_{2/3}\text{Sc}_{1/3})_2\text{AlC}$  and  $(\text{W}_{2/3}\text{Y}_{1/3})_2\text{AlC}$  *i*-MAX phases.<sup>[27]</sup> Free-standing  $\text{W}_{1.33}\text{C}$  electrodes, with a thickness of  $2\text{--}4 \mu\text{m}$ , were prepared as composites with PEDOT:PSS (10 wt%), and were evaluated in  $1 \text{ M H}_2\text{SO}_4$  electrolyte. The normalized capacitance of  $2 \mu\text{m}$ -thick  $\text{W}_{1.33}\text{C}(\text{Sc})/\text{PEDOT:PSS}$  and  $\text{W}_{1.33}\text{C}(\text{Y})/\text{PEDOT:PSS}$  electrodes were found to be  $610 \text{ F cm}^{-3}$  ( $116 \text{ F g}^{-1}$ ) and  $591 \text{ F cm}^{-3}$  ( $191 \text{ F g}^{-1}$ ) at the scan rate of  $5 \text{ mV s}^{-1}$ , respectively. Similar to Mo-based *i*-MXene, the  $\text{W}_{1.33}\text{C}$  *i*-MXene, derived from the Y-containing parent phase, rendered slightly lower charge storage capacitance compared to the Sc-containing counterpart. Also, the charge storage mechanism in W-based *i*-MXenes was found to be mainly dominated by the surface-controlled capacitive behavior, with the CV curves not exhibiting distinct redox peaks.

While *i*-MXenes are characterized by ordered vacancies, the as-synthesized  $\text{Nb}_{1.33}\text{C}$  MXene, derived from the quaternary solid-solution  $(\text{Nb}_{2/3}\text{Sc}_{1/3})_2\text{AlC}$  MAX phase, possesses disordered vacancies and small vacancy clusters ( $0.1\text{--}2 \text{ nm}$ ) due to the removal of the alloying Sc atoms. However, the charge storage behavior of  $\text{Nb}_{1.33}\text{C}$  MXene has to date not been reported. Herein, we present the capacitive performance of a  $\text{Nb}_{1.33}\text{C}$  “paper” electrode in  $1 \text{ M H}_2\text{SO}_4$  electrolyte by measuring CV and galvanostatic charge/discharge curves at different scan

rates and current densities, see Figure 9a. The  $\text{Nb}_{1.33}\text{C}$  MXene exhibits a gravimetric capacitance of  $75 \text{ F g}^{-1}$  and volumetric capacitance of  $325 \text{ F cm}^{-3}$ , however, both of these values are far below those reported for the Mo-based *i*-MXene. Still, a more valid comparison would be between the supercapacitive performance of  $\text{Nb}_2\text{C}$  and  $\text{Nb}_{1.33}\text{C}$ , though there is no published data for  $\text{Nb}_2\text{C}$  allowing such comparison. However,  $\text{Nb}_2\text{C}$  MXene has been studied as an anode material in Li-ion batteries, rendering a reversible capacity of  $600 \text{ mAh g}^{-1}$  at  $0.1 \text{ C}$ .<sup>[50]</sup>

Interestingly, the  $\text{Nb}_{1.33}\text{C}$  “paper” electrode exhibits rectangular CV curves in the voltage window of  $-0.1\text{--}0.45 \text{ V}$  (vs Ag/AgCl), whereas the major capacitive contribution in Mo- and W-based MXenes is rendered in a more negative voltage window. For instance, a  $\text{Mo}_{1.33}\text{C}$  “paper” electrode has been cycled in the voltage window of  $-0.35\text{--}0.30 \text{ V}$  (vs Ag/AgCl) and a  $\text{W}_{1.33}\text{C}$  “paper” electrode has been characterized in the voltage window of  $-0.25\text{--}0.20 \text{ V}$  (vs Ag/AgCl). Hence, despite the lower capacitance,  $\text{Nb}_{1.33}\text{C}$  can be an interesting platform for the development of positive electrode materials. It should be noted that the  $\text{Nb}_{1.33}\text{C}$  MXene retained almost 100% of the initial capacitance after 10000 charge/discharge cycles, see Figure 9b, which is of great significance for positive electrode materials.

## 5. *i*-MXenes as Catalysts for Hydrogen Evolution Reaction

It has been demonstrated that MXenes are promising catalysts in chemical or electrochemical reactions due to their thermal stability, intrinsic metallic conductivity, electrochemical activity, and specific surface structure, including edges, surface terminations, and vacancies.<sup>[42,51]</sup> For instance, Pan et al.<sup>[52]</sup> have employed DFT calculations to estimate  $\text{H}_2$  adsorption free energy of  $\text{W}_2\text{C}$  and  $\text{Mo}_2\text{C}$  MXenes, indicating excellent hydrogen evolution reaction (HER) activity. Moreover,  $\text{Mo}_2\text{C}$  MXene exhibited high catalytic activity towards HER.

In the case of *i*-MXenes, the preliminary results revealed that  $\text{W}_{1.33}\text{C}$  is a promising catalyst for HER.<sup>[22]</sup> The HER activity of W-based *i*-MXene has been compared with  $\text{Mo}_{1.33}\text{C}$  *i*-MXene and Pt/carbon catalysts, as shown in Figure 10. Both as-synthesized  $\text{Mo}_{1.33}\text{C}$  and  $\text{W}_{1.33}\text{C}$  exhibited similar overpotential for HER, which for an initial study shows a very respectable  $\approx 320 \text{ mV}$

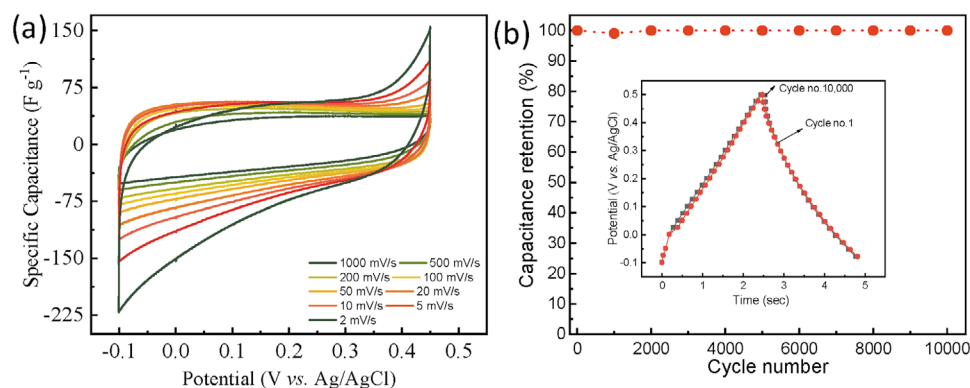


**Figure 9.** Electrochemical performance of  $\text{Nb}_{1.33}\text{C}$  MXene: a) CV curves at different scan rates and b) cyclic stability and charge/discharge curves (1<sup>st</sup> and 10000<sup>th</sup> cycles).

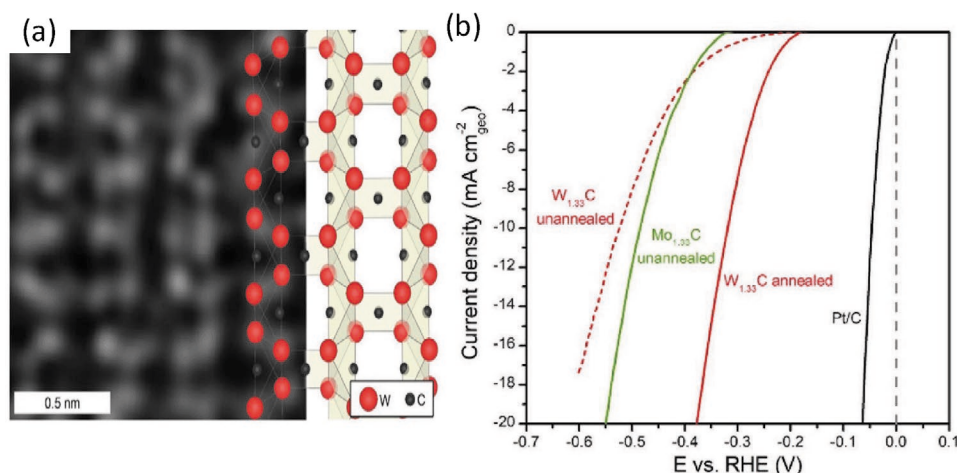


**Figure 10.** Catalytic behavior of  $W_{1.33}C$  MXene: a) atomically resolved image with overlaid schematic atomic structure model and b) HER polarization curves for  $Mo_{1.33}C$  (green), unannealed  $W_{1.33}C$  (dashed red), annealed  $W_{1.33}C$  (red), and Pt/C (black) recorded in  $H_2$  saturated 0.1 M  $HClO_4$  at room temperature. Reproduced with permission.<sup>[22]</sup> Copyright 2018, Wiley-VCH.

at a current density of  $10 \text{ mA cm}^{-2}$ . Moreover, the influence of high-temperature annealing on the catalytic activity of  $W_{1.33}C$  has also been studied, exhibiting a significant decrease in overpotential after annealing at  $700^\circ\text{C}$  in  $H_2$  (3%)/Ar for 1 h. This is yet another indication that post-etch processing is a crucial step in modulating the MXene performance in supercapacitive and catalytic applications.

Most recently, we have carried out a detailed experimental and theoretical study to explore the potential of different MXene/*i*-MXenes, such as  $Mo_{1.33}C$ ,  $Nb_{1.33}C$ , and  $W_{1.33}C$ , as catalysts for HER. In particular for  $W_{1.33}C$ , we have investigated the theoretical hydrogen adsorption on the surface as well as inside the vacancies of the *i*-MXenes, to demonstrate the potential influence of vacancies on the catalytic behavior. The preliminary results indicate that in addition to inherent compositional variations, the catalytic activity of the *i*-MXenes can be tuned by post-etching surface treatments, altering the surface chemistry.

## 6. Conclusion and Outlook

In summary, the *in-plane* chemical order and selective removal of both  $M^{2-}$  and A-elements from  $(M^{1.2/3}M^{2.1/3})_2AC$  *i*-MAX phases result in *i*-MXenes with ordered divacancies, rendering promise for a range of applications, including energy storage and catalysis. Moreover, the shown incorporation of non-conventional MAX phase elements at the  $M^1$  and  $M^2$  sites suggest the possibility of forming a wide range of novel MXene compositions, for different applications, by using the concept of “targeted etching”, which is detailing the chemical etching procedures to obtain either a vacancies-containing MXene or a chemically-ordered MXene from the same parent material.

The first member of the *i*-MXene family,  $Mo_{1.33}C$ , has been extensively investigated as electrode material in symmetric and asymmetric supercapacitors, whereas another *i*-MXene,  $W_{1.33}C$ , has shown promise as a catalyst for HER. This report summarizes the published results on supercapacitive and catalytic performance of Mo- and W-based *i*-MXenes, and presents new results from our most recent investigations on post-etching

processing of  $Mo_{1.33}C$  for enhanced charge storage. We report that simple annealing (in Ar) of the *d*- $Mo_{1.33}C$  “paper” electrode renders a superior volumetric capacitance of  $1635 \text{ F cm}^{-3}$  at a scan rate of  $2 \text{ mV s}^{-1}$ , which is 42% higher than the as-prepared *d*- $Mo_{1.33}C$  “paper” electrode, and the highest reported capacitance for MXene-based electrodes to date. These preliminary results clearly show that the charge storage performance of *i*-MXenes can be further increased by post-etch processing. Moreover, we report that different cations can be intercalated between  $Mo_{1.33}C$  nanosheets, motivating further work to establish the relationships between cationic characteristics and intercalation behavior. Finally, we also present initial analysis of the charge storage behavior for  $Nb_{1.33}C$  MXene with disordered vacancies (i.e., not an *i*-MXene), which suggests further studies in the direction of potential positive electrode materials. It is worth emphasizing that *i*-MXenes, in general, exhibit excellent cyclic stability in aqueous electrolytes, which makes them highly promising for supercapacitive and HER applications. Currently, we are exploring the potential of *i*-MXenes in non-aqueous electrolytes and secondary-ion battery applications.

In summary, the unique surface structure of *i*-MXenes, possessing ordered divacancies, plays a vital role in endowing superior charge storage and catalytic performance. Further investigations on the influence of the vacancies on the material's properties are highly motivated, for an increased fundamental understanding and widespread utilization of these materials in practical applications. Moreover, in addition to the construction of *i*-MXene based symmetric and asymmetric devices, the potential of *i*-MXenes should be explored for secondary-ion batteries and metal-ion capacitors.

## Acknowledgements

B.A. and A.E.G. contributed equally to this work. B.A. acknowledges the research grant from Wenner-Gren Stiftelserna (UPD2017-0171). Also, support from the Knut and Alice Wallenberg's Foundation (a Fellowship/Scholar grant) and the Swedish Foundation for Strategic Research (a Synergy grant) is acknowledged. The authors finally acknowledge the support from the Swedish Government Strategic Research Area



in Materials Science on Functional Materials at Linköping University (Faculty Grant SFO-Mat-LiU No 2009 00971) and Vinnova and the Swedish Strategy Group for EU-Coordination (2018-02677).

## Conflict of Interest

The authors declare no conflict of interest.

## Keywords

catalysis, energy storage, hydrogen evolution reaction, MXenes, supercapacitors

Received: January 30, 2020

Revised: March 19, 2020

Published online:

- [1] a) H. Tamaki, H. K. Sato, T. Kanno, *Adv. Mater.* **2016**, *28*, 10182; b) J. A. Mundy, C. M. Brooks, M. E. Holtz, J. A. Moyer, H. Das, A. F. Rebola, J. T. Heron, J. D. Clarkson, S. M. Disseler, Z. Liu, A. Farhan, R. Held, R. Hovden, E. Padgett, Q. Mao, H. Paik, R. Misra, L. F. Kourkoutis, E. Arenholz, A. Scholl, J. A. Borchers, W. D. Ratcliff, R. Ramesh, C. J. Fennie, P. Schiffer, D. A. Muller, D. G. Schlom, *Nature* **2016**, *537*, 523; c) B. Anasori, M. R. Lukatskaya, Y. Gogotsi, *Nat. Rev. Mater.* **2017**, *2*, 16098; d) M. Ghidui, M. R. Lukatskaya, M. Q. Zhao, Y. Gogotsi, M. W. Barsoum, *Nature* **2014**, *516*, 78; e) N. Kurra, B. Ahmed, Y. Gogotsi, H. N. Alshareef, *Adv. Energy Mater.* **2016**, *6*, 1601372.
- [2] L. D. Zhao, S. H. Lo, Y. Zhang, H. Sun, G. Tan, C. Uher, C. Wolverton, V. P. Dravid, M. G. Kanatzidis, *Nature* **2014**, *508*, 373.
- [3] a) X. Y. Chia, M. Pumera, *Nat. Catal.* **2018**, *1*, 909; b) D. Deng, K. S. Novoselov, Q. Fu, N. Zheng, Z. Tian, X. Bao, *Nat. Nanotechnol.* **2016**, *11*, 218.
- [4] W. Eerenstein, N. D. Mathur, J. F. Scott, *Nature* **2006**, *442*, 759.
- [5] a) M. Sokol, V. Natu, S. Kota, M. W. Barsoum, *Trends Chem.* **2019**, *1*, 210; b) M. W. Barsoum, *Prog. Solid State Chem.* **2000**, *28*, 201.
- [6] a) M. Naguib, M. Kurtoglu, V. Presser, J. Lu, J. Niu, M. Heon, L. Hultman, Y. Gogotsi, M. W. Barsoum, *Adv. Mater.* **2011**, *23*, 4248; b) M. Naguib, O. Mashtalir, J. Carle, V. Presser, J. Lu, L. Hultman, Y. Gogotsi, M. W. Barsoum, *ACS Nano* **2012**, *6*, 1322.
- [7] a) P. Eklund, M. Beckers, U. Jansson, H. Högberg, L. Hultman, *Thin Solid Films* **2010**, *518*, 1851; b) M. W. Barsoum, T. El-Raghy, *Am. Sci.* **2001**, *89*, 334.
- [8] a) A.-S. Farle, C. Kwakernaak, S. van der Zwaag, W. G. Sloof, *J. Eur. Ceram. Soc.* **2015**, *35*, 37; b) W. G. Sloof, R. Pei, S. A. McDonald, J. L. Fife, L. Shen, L. Boatemaa, A. S. Farle, K. Yan, X. Zhang, S. van der Zwaag, P. D. Lee, P. J. Withers, *Sci. Rep.* **2016**, *6*, 23040; c) M. Barsoum, T. Zhen, S. Kalidindi, M. Radovic, A. Murugaiah, *Nat. Mater.* **2003**, *2*, 107; d) A. Mockute, M. Dahlqvist, J. Emmerlich, L. Hultman, J. M. Schneider, P. O. Persson, J. Rosén, *Phys. Rev. B* **2013**, *87*, 094113.
- [9] a) A. S. Ingason, A. Mockute, M. Dahlqvist, F. Magnus, S. Olafsson, U. B. Arnalds, B. Alling, I. A. Abrikosov, B. Hjorvarsson, P. O. Persson, J. Rosen, *Phys. Rev. Lett.* **2013**, *110*, 195502; b) M. A. Pietzka, J. C. Schuster, *J. Am. Ceram. Soc.* **1996**, *79*, 2321; c) S. Kerdsonpanya, K. Buchholt, O. Tengstrand, J. Lu, J. Jensen, L. Hultman, P. Eklund, *J. Appl. Phys.* **2011**, *110*, 053516; d) T. Cabioch, P. Eklund, V. Mauchamp, M. Jaouen, M. W. Barsoum, *J. Eur. Ceram. Soc.* **2013**, *33*, 897; e) A. Talapatra, T. Duong, W. Son, H. Gao, M. Radovic, R. Arróyave, *Phys. Rev. B* **2016**, *94*, 104106; f) M. Ashton, R. G. Hennig, S. R. Broderick, K. Rajan, S. B. Sinnott, *Phys. Rev. B* **2016**, *94*, 054116.
- [10] a) F. L. Meng, Y. C. Zhou, J. Y. Wang, *Scr. Mater.* **2005**, *53*, 1369; b) J. Rosén, M. Dahlqvist, S. Simak, D. McKenzie, M. Bilek, *Appl. Phys. Lett.* **2010**, *97*, 073103; c) M. Dahlqvist, B. Alling, I. A. Abrikosov, J. Rosen, *Phys. Rev. B* **2011**, *84*, 220403; d) J. Rosen, P. Å. Persson, M. Ionescu, A. Kondyurin, D. McKenzie, M. Bilek, *Appl. Phys. Lett.* **2008**, *92*, 064102; e) D. Horlait, S. C. Middleburgh, A. Chroneos, W. E. Lee, *Sci. Rep.* **2016**, *6*, 18829.
- [11] A. Mockute, P. O. Å. Persson, F. Magnus, A. S. Ingason, S. Olafsson, L. Hultman, J. Rosen, *Phys. Status Solidi RRL* **2014**, *8*, 420.
- [12] R. Salikhov, R. Meshkian, D. Weller, B. Zingsem, D. Spoddig, J. Lu, A. S. Ingason, H. Zhang, J. Rosen, U. Wiedwald, M. Farle, *J. Appl. Phys.* **2017**, *121*, 163904.
- [13] a) M. Dahlqvist, J. Rosen, *Phys. Chem. Chem. Phys.* **2015**, *17*, 31810; b) J. Rosen, M. Dahlqvist, Q. Tao, L. Hultman, in *2D Metal Carbides and Nitrides (MXenes)* (Eds: B. Anasori, Y. Gogotsi), Springer International Publishing, Cham **2019**, p. 37.
- [14] a) Z. Liu, E. Wu, J. Wang, Y. Qian, H. Xiang, X. Li, Q. Jin, G. Sun, X. Chen, J. Wang, *Acta Mater.* **2014**, *73*, 186; b) Z. Liu, L. Zheng, L. Sun, Y. Qian, J. Wang, M. Li, *J. Am. Ceram. Soc.* **2014**, *97*, 67.
- [15] a) B. Anasori, M. Dahlqvist, J. Halim, E. J. Moon, J. Lu, B. C. Hosler, E. N. Caspi, S. J. May, L. Hultman, P. Eklund, J. Rosen, M. W. Barsoum, *J. Appl. Phys.* **2015**, *118*, 094304; b) B. Anasori, J. Halim, J. Lu, C. A. Voigt, L. Hultman, M. W. Barsoum, *Scr. Mater.* **2015**, *101*, 5.
- [16] a) M. Dahlqvist, A. Petruhins, J. Lu, L. Hultman, J. Rosen, *ACS Nano* **2018**, *12*, 7761; b) M. Dahlqvist, J. Lu, R. Meshkian, Q. Tao, L. Hultman, J. Rosen, *Sci. Adv.* **2017**, *3*, e1700642.
- [17] Q. Tao, M. Dahlqvist, J. Lu, S. Kota, R. Meshkian, J. Halim, J. Palisaitis, L. Hultman, M. W. Barsoum, P. O. A. Persson, J. Rosen, *Nat. Commun.* **2017**, *8*, 14949.
- [18] R. Meshkian, Q. Z. Tao, M. Dahlqvist, J. Lu, L. Hultman, J. Rosen, *Acta Mater.* **2017**, *125*, 476.
- [19] A. Mockute, Q. Tao, M. Dahlqvist, J. Lu, S. Calder, E. N. Caspi, L. Hultman, J. Rosen, *Phys. Rev. Mater.* **2019**, *3*, 113607.
- [20] J. Lu, A. Thore, R. Meshkian, Q. Tao, L. Hultman, J. Rosen, *Cryst. Growth Des.* **2017**, *17*, 5704.
- [21] J. Thörnberg, J. Halim, J. Lu, R. Meshkian, J. Palisaitis, L. Hultman, P. O. Persson, J. Rosen, *Nanoscale* **2019**, *11*, 14720.
- [22] R. Meshkian, M. Dahlqvist, J. Lu, B. Wickman, J. Halim, J. Thörnberg, Q. Tao, S. Li, S. Intikhab, J. Snyder, M. W. Barsoum, M. Yildizhan, J. Palisaitis, L. Hultman, P. O. A. Persson, J. Rosen, *Adv. Mater.* **2018**, *30*, 1706409.
- [23] L. Chen, M. Dahlqvist, T. Lapauw, B. Tunca, F. Wang, J. Lu, R. Meshkian, K. Lambrinou, B. Blanpain, J. Vleugels, J. Rosen, *Inorg. Chem.* **2018**, *57*, 6237.
- [24] a) Q. Z. Tao, J. Lu, M. Dahlqvist, A. Mockute, S. Calder, A. Petruhins, R. Meshkian, O. Rivin, D. Potashnikov, E. N. Caspi, H. Shaked, A. Hoser, C. Opagiste, R. M. Galera, R. Salikhov, U. Wiedwald, C. Ritter, A. R. Wildes, B. Johansson, L. Hultman, M. Fade, M. W. Barsoum, J. Rosen, *Chem. Mater.* **2019**, *31*, 2476; b) A. Petruhins, J. Lu, L. Hultman, J. Rosen, *Mater. Res. Lett.* **2019**, *7*, 446.
- [25] a) I. P. Novoselova, A. Petruhins, U. Wiedwald, Å. S. Ingason, T. Hase, F. Magnus, V. Kapaklis, J. Palisaitis, M. Spasova, M. Farle, *Sci. Rep.* **2018**, *8*, 2637; b) I. P. Novoselova, A. Petruhins, U. Wiedwald, D. Weller, J. Rosen, M. Farle, R. Salikhov, *Mater. Res. Lett.* **2019**, *7*, 159.
- [26] A. Petruhins, M. Dahlqvist, J. Lu, L. Hultman, J. Rosen, *Cryst. Growth Des.* **2019**, *20*, 55.
- [27] R. Meshkian, H. Lind, J. Halim, A. El Ghazaly, J. Thörnberg, Q. Tao, M. Dahlqvist, J. Palisaitis, P. O. Å. Persson, J. Rosen, *ACS Appl. Nano Mater.* **2019**, *2*, 6209.
- [28] I. Persson, A. El Ghazaly, Q. Tao, J. Halim, S. Kota, V. Darakchieva, J. Palisaitis, M. W. Barsoum, J. Rosen, P. O. A. Persson, *Small* **2018**, *14*, 1703676.

- [29] E. N. Hoffman, G. Yushin, M. W. Barsoum, Y. Gogotsi, *Chem. Mater.* **2005**, *17*, 2317.
- [30] a) B. Ahmed, D. H. Anjum, M. N. Hedhili, Y. Gogotsi, H. N. Alshareef, *Nanoscale* **2016**, *8*, 7580; b) M. Naguib, O. Mashtalir, M. R. Lukatskaya, B. Dyatkin, C. Zhang, V. Presser, Y. Gogotsi, M. W. Barsoum, *Chem. Commun.* **2014**, *50*, 7420.
- [31] T. Su, R. Peng, Z. D. Hood, M. Naguib, I. N. Ivanov, J. K. Keum, Z. Qin, Z. Guo, Z. Wu, *ChemSusChem* **2018**, *11*, 688.
- [32] Z. Wang, K. Yu, Y. Feng, R. Qi, J. Ren, Z.-Q. Zhu, *ACS Appl. Mater. Interfaces* **2019**, *11*, 44282.
- [33] B. Ahmed, D. H. Anjum, Y. Gogotsi, H. N. Alshareef, *Nano Energy* **2017**, *34*, 249.
- [34] J. Halim, J. Palisaitis, J. Lu, J. Thörnberg, E. J. Moon, M. Precner, P. Eklund, P. O. Å. Persson, M. W. Barsoum, J. Rosen, *ACS Appl. Nano Mater.* **2018**, *1*, 2455.
- [35] H. Lind, J. Halim, S. I. Simak, J. Rosen, *Phys. Rev. Mater.* **2017**, *1*, 044002.
- [36] J. Halim, E. J. Moon, P. Eklund, J. Rosen, M. W. Barsoum, T. Ouisse, *Phys. Rev. B* **2018**, *98*, 104202.
- [37] a) R. B. Rakhi, B. Ahmed, D. Anjum, H. N. Alshareef, *ACS Appl. Mater. Interfaces* **2016**, *8*, 18806; b) R. B. Rakhi, B. Ahmed, M. N. Hedhili, D. H. Anjum, H. N. Alshareef, *Chem. Mater.* **2015**, *27*, 5314.
- [38] a) Y. Dall'Agnese, P. L. Taberna, Y. Gogotsi, P. Simon, *J. Phys. Chem. Lett.* **2015**, *6*, 2305; b) X. Zhang, L. Wang, W. Liu, C. Li, K. Wang, Y. Ma, *ACS Omega* **2020**, *5*, 75; c) Y. Zhao, J. Guo, A. Liu, T. Ma, *J. Alloys Compd.* **2020**, *814*, 152271; d) X. Wang, H. Li, H. Li, S. Lin, J. Bai, J. M. Dai, C. H. Liang, X. B. Zhu, Y. P. Sun, S. X. Dou, *J. Mater. Chem. A* **2019**, *7*, 2291; e) J. Come, M. Naguib, P. Rozier, M. W. Barsoum, Y. Gogotsi, P. L. Taberna, M. Morcrette, P. Simon, *J. Electrochem. Soc.* **2012**, *159*, A1368.
- [39] a) X. Zhang, J. Li, J. Li, L. Han, T. Lu, X. Zhang, G. Zhu, L. Pan, *Chem. Eng. J.* **2020**, *385*, 123394; b) D. Xu, K. Ma, L. Chen, Y. Hu, H. Jiang, C. Li, *Chem. Eng. Sci.* **2020**, *212*, 115342; c) B. P. Thapaliya, C. J. Jafta, H. Lyu, J. Xia, H. M. Meyer III, M. P. Paranthaman, X. G. Sun, C. A. Bridges, S. Dai, *ChemSusChem* **2019**, *12*, 1316; d) Z. Ma, X. Zhou, W. Deng, D. Lei, Z. Liu, *ACS Appl. Mater. Interfaces* **2018**, *10*, 3634; e) M. Lu, H. Li, W. Han, J. Chen, W. Shi, J. Wang, X.-M. Meng, J. Qi, H. Li, B. Zhang, W. Zhang, W. Zheng, *J. Energy Chem.* **2019**, *31*, 148; f) R. Cheng, T. Hu, H. Zhang, C. Wang, M. Hu, J. Yang, C. Cui, T. Guang, C. Li, C. Shi, P. Hou, X. Wang, *J. Phys. Chem. C* **2019**, *123*, 1099; g) C. Chen, X. Xie, B. Anasori, A. Sarycheva, T. Makaryan, M. Zhao, P. Urbankowski, L. Miao, J. Jiang, Y. Gogotsi, *Angew. Chem., Int. Ed.* **2018**, *57*, 1846; h) M. Q. Zhao, M. Torelli, C. E. Ren, M. Ghidui, Z. Ling, B. Anasori, M. W. Barsoum, Y. Gogotsi, *Nano Energy* **2016**, *30*, 603; i) M. Naguib, J. Come, B. Dyatkin, V. Presser, P. L. Taberna, P. Simon, M. W. Barsoum, Y. Gogotsi, *Electrochem. Commun.* **2012**, *16*, 61; j) B. Ahmed, C. Xia, H. N. Alshareef, *Nano Today* **2016**, *11*, 250.
- [40] a) F. Shahzad, M. Alhabeb, C. B. Hatter, B. Anasori, S. Man Hong, C. M. Koo, Y. Gogotsi, *Science* **2016**, *353*, 1137; b) X. L. Li, X. W. Yin, S. Liang, M. H. Li, L. F. Cheng, L. T. Zhang, *Carbon* **2019**, *146*, 210; c) Q.-W. Wang, H.-B. Zhang, J. Liu, S. Zhao, X. Xie, L. Liu, R. Yang, N. Koratkar, Z.-Z. Yu, *Adv. Funct. Mater.* **2019**, *29*, 1806819; d) X. L. Li, X. W. Yin, M. K. Han, C. Q. Song, X. N. Sun, H. L. Xu, L. F. Cheng, L. T. Zhang, *J. Mater. Chem. C* **2017**, *5*, 7621.
- [41] a) A. A. Shamsabadi, M. S. Gh, B. Anasori, M. Soroush, *ACS Sustainable Chem. Eng.* **2018**, *6*, 16586; b) F. Alimohammadi, M. S. Gh, N. H. Attanayake, A. C. Thenuwara, Y. Gogotsi, B. Anasori, D. R. Strongin, *Langmuir* **2018**, *34*, 7192; c) K. Rasool, M. Helal, A. Ali, C. E. Ren, Y. Gogotsi, K. A. Mahmoud, *ACS Nano* **2016**, *10*, 3674.
- [42] a) J. Qin, X. Hu, X. Li, Z. Yin, B. Liu, K.-h. Lam, *Nano Energy* **2019**, *61*, 27; b) P. Kuang, M. He, B. Zhu, J. Yu, K. Fan, M. Jaroniec, *J. Catal.* **2019**, *375*, 118379; c) L. Cheng, Q. Chen, J. Li, H. Liu, *Appl. Catal., B* **2020**, *267*, 8, <https://doi.org/10.1016/j.apcatb.2019.118379>; d) W. T. Tysoe, *Nat. Catal.* **2018**, *1*, 316; e) J. Y. Diao, M. M. Hu, Z. Lian, Z. J. Li, H. Zhang, F. Huang, B. Li, X. H. Wang, D. S. Su, H. Y. Liu, *ACS Catal.* **2018**, *8*, 10051.
- [43] a) X. Y. Peng, Y. L. Zhang, D. T. Lu, Y. J. Guo, S. J. Guo, *Sens. Actuators, B* **2019**, *286*, 222; b) H. An, T. Habib, S. Shah, H. L. Gao, A. Patel, I. Echols, X. F. Zhao, M. Radovic, M. J. Green, J. L. Lutkenhaus, *ACS Appl. Nano Mater.* **2019**, *2*, 948; c) Y. Ma, Y. Yue, H. Zhang, F. Cheng, W. Zhao, J. Rao, S. Luo, J. Wang, X. Jiang, Z. Liu, N. Liu, Y. Gao, *ACS Nano* **2018**, *12*, 3209; d) Y. F. Fang, X. C. Yang, T. Chen, G. F. Xu, M. L. Liu, J. Q. Liu, Y. H. Xu, *Sens. Actuators, B* **2018**, *263*, 400.
- [44] a) R. Meshkian, L. A. Naslund, J. Halim, J. Lu, M. W. Barsoum, J. Rosen, *Scr. Mater.* **2015**, *108*, 147; b) J. Halim, S. Kota, M. R. Lukatskaya, M. Naguib, M.-Q. Zhao, E. J. Moon, J. Pitcock, J. Nanda, S. J. May, Y. Gogotsi, M. W. Barsoum, *Adv. Funct. Mater.* **2016**, *26*, 3118.
- [45] M. R. Lukatskaya, O. Mashtalir, C. E. Ren, Y. Dall'Agnese, P. Rozier, P. L. Taberna, M. Naguib, P. Simon, M. W. Barsoum, Y. Gogotsi, *Science* **2013**, *341*, 1502.
- [46] T. X. Shang, Z. F. Lin, C. S. Qi, X. C. Liu, P. Li, Y. Tao, Z. T. Wu, D. W. Li, P. Simon, Q. H. Yang, *Adv. Funct. Mater.* **2019**, *29*, 1903960.
- [47] a) M. R. Lukatskaya, S. Kota, Z. F. Lin, M. Q. Zhao, N. Shpigel, M. D. Levi, J. Halim, P. L. Taberna, M. Barsoum, P. Simon, Y. Gogotsi, *Nat. Energy* **2017**, *2*, 17105; b) X. Y. Lang, B. T. Liu, X. M. Shi, Y. Q. Li, Z. Wen, Q. Jiang, *Adv. Sci.* **2016**, *3*, 1500319; c) M. F. El-Kady, M. Ihns, M. Li, J. Y. Hwang, M. F. Mousavi, L. Chaney, A. T. Lech, R. B. Kaner, *Proc. Natl. Acad. Sci. USA* **2015**, *112*, 4233.
- [48] L. Qin, Q. Tao, A. El Ghazaly, J. Fernandez-Rodriguez, P. O. Å. Persson, J. Rosen, F. Zhang, *Adv. Funct. Mater.* **2018**, *28*, 1703808.
- [49] L. Qin, Q. Tao, X. Liu, M. Fahlman, J. Halim, P. O. Persson, J. Rosen, F. Zhang, *Nano Energy* **2019**, *60*, 734.
- [50] O. Mashtalir, M. R. Lukatskaya, M. Q. Zhao, M. W. Barsoum, Y. Gogotsi, *Adv. Mater.* **2015**, *27*, 3501.
- [51] a) C. Zhao, C. Qiu, S. Deng, X. Sun, Y. Gao, Y. Cao, H. Zhuo, G. Zhuang, X. Zhong, Z. Wei, Z. Yao, J.-g. Wang, *Appl. Surf. Sci.* **2019**, *481*, 554; b) Y. Gao, Y. Cao, H. Zhuo, X. Sun, Y. Gu, G. Zhuang, S. Deng, X. Zhong, Z. Wei, X. Li, J.-g. Wang, *Catal. Today* **2020**, *339*, 120; c) G. P. Gao, A. P. O'Mullane, A. J. Du, *ACS Catal.* **2017**, *7*, 494; d) R. Xiao, C. Zhao, Z. Zou, Z. Chen, L. Tian, H. Xu, H. Tang, Q. Liu, Z. Lin, X. Yang, *Appl. Catal., B* **2019**, <https://doi.org/10.1016/j.apcatb.2019.118382>; e) C. Liu, Q. X. Xu, Q. F. Zhang, Y. S. Zhu, M. W. Ji, Z. W. Tong, W. H. Hou, Y. Zhang, J. G. Xu, *J. Mater. Sci.* **2019**, *54*, 2458; f) H. L. Zhang, M. Li, J. L. Cao, Q. J. Tang, P. Kang, C. X. Zhu, M. J. Ma, *Ceram. Int.* **2018**, *44*, 19958; g) Z. M. Wong, T. L. Tan, S. W. Yang, G. Q. Xu, *ACS Appl. Mater. Interfaces* **2018**, *10*, 39879; h) K. K. Li, T. F. Jiao, R. R. Xing, G. D. Zou, J. X. Zhou, L. X. Zhang, Q. M. Peng, *Sci. China Mater.* **2018**, *61*, 728; i) C. Peng, H. J. Wang, H. Yu, F. Peng, *Mater. Res. Bull.* **2017**, *89*, 16.
- [52] Y. L. Bai, K. Zhou, N. Srikanth, J. H. L. Pang, X. D. He, R. G. Wang, *RSC Adv.* **2016**, *6*, 35731.